Microchimica Acta (2021) 188:78
https://doi.org/10.1007/s00604-021-04735-y

ORIGINAL PAPER

Sensitive sandwich-type voltammetric immunosensor for breast cancer biomarker HER2 detection based on gold nanoparticles decorated Cu-MOF and Cu_2ZnSnS_4 NPs/Pt/g-C_3N_4 composite

Mehmet Lütfi Yola[1]

Received: 17 December 2020 / Accepted: 27 January 2021

Abstract

A sandwich-type sensitive voltammetric immunosensor for breast cancer biomarker human epidermal growth factor receptor 2 (HER2) detection was prepared. The electrochemical immunosensor was developed based on gold nanoparticles decorated copper-organic framework (AuNPs/Cu-MOF) and quaternary chalcogenide with platinum-doped graphitic carbon nitride (g-C_3N_4). Cu_2ZnSnS_4 nanoparticle (CZTS NP) quaternary chalcogenide with platinum (Pt)-doped g-C_3N_4 composite (Pt/g-C_3N_4) was tagged as CZTS NPs/Pt/g-C_3N_4. AuNPs/Cu-MOF composite was successfully synthesized by amidation reaction between AuNPs functionalized with amino group and Cu-MOFs containing carboxylic acid. After the conjugations of primer HER2 antibody and antigen HER2 protein to AuNPs/Cu-MOF as sensor platform, CZTS NPs/Pt/g-C_3N_4 composite was prepared by one-pot hydrothermal method. After immune reaction of 30 min, the prepared HER2 immunosensor was characterized by transmission electron microscopy (TEM), scanning electron microscopy (SEM), x-ray diffraction (XRD) method, x-ray photoelectron spectroscopy (XPS), Fourier transform infrared spectroscopy (FTIR), cyclic voltammetry (CV), and electrochemical impedance spectroscopy (EIS). The developed immunosensor showed high sensitivity with a detection limit of 3.00 fg mL^{-1}. Additional properties of the voltammetric immunosensor are high selectivity, stability, reproducibility, and reusability.

Keywords Breast cancer biomarker · Immunosensor · Voltammetry · Quaternary chalcogenide · MOF

Introduction

HER2 can facilitate excessive breast cancer cell growth and is one of the most significant diagnostic biomarkers. The development of about 35% of breast cancer tumors is mainly corresponded to HER2's overexpression [1]. These HER2-positive breast cancers are responsible for about 35% of breast cancers. Hence, HER2's fast analysis improves the effectiveness of treatment [2, 3]. According to literature, while HER2 content in the blood of healthy people is between 2.0 and 15.0 ng mL^{-1}, the amount of HER2 increases up to 75.0 ng mL^{-1} in breast cancer patients [4, 5]. Lately, the fluorescent-based detection methods including in situ hybridization (FISH) have been utilized for HER2 gene expression to determine the presence of HER2 protein on the cell. Nonetheless, the biopsy tissue exemplification and expensive instruments can be needed in immunohistochemistry (IHC) and FISH methods, causing a limited application for HER2 recognition [6, 7]. Hence, the simple and sensitive analysis techniques are of great importance for HER2 recognition. Lately, the new-type immunosensors based on voltammetry started to attract great attention in the terms of high selectivity, sensitivity, and low cost [8–15]. Even, some voltammetric biosensors for HER2 recognition have presented by using different nanoparticle systems [16, 17]. There are two-type voltammetric immunosensors including sandwich type containing label and label-free. To obtain sensitive biosensor signals, the sandwich-type immunosensors are especially used and applied to the complex samples [18]. In the preparation of sandwich-type immunosensors, the primer (capture) antibody is firstly immobilized to any sensor platform such as electrochemical surface. Then, the analyte (target) antigen sandwiched between the primer and detection (seconder) antibodies. However, the type of nanomaterial/composite conjugated capture and seconder antibodies is very important to observe the sensitive sensor signals [9]. For example, label-

✉ Mehmet Lütfi Yola
mlutfi.yola@hku.edu.tr

[1] Faculty of Health Sciences, Department of Nutrition and Dietetics, Hasan Kalyoncu University, Gaziantep, Turkey

Published online: 10 February 2021

free electrochemical immunosensor based on Fe_3O_4 nanoparticles into an amino-functionalized MOF (Fe_3O_4@TMU-21) and multi-walled carbon nanotubes was prepared for HER2 detection. Thus, a linear relation of 1.00–100.00 ng mL^{-1} and detection limit (LOD) of 0.30 pg mL^{-1} were recorded [3]. Secondly, cerium oxide-monoclonal antibody bioconjugate-based electrochemical immunosensing was performed for HER2. After the immobilization of this bioconjugate on a carbon-AuNPs electrode, the prepared immunosensor was applied to human serum plasma, and LOD of 34.90 pg mL^{-1} was obtained [19]. Then, lead sulfide quantum dots-conjugated secondary HER2 antibody (Ab_2-PbS QDs) was designed and used for electrochemical immunosensing of HER2. The developed immunosensor demonstrated a linear relation of 1.00–100.00 ng mL^{-1} and LOD of 0.28 ng mL^{-1} [20]. In other study, DNA self-assembly amplification generating electric current was developed for HER2 detection. In this study, a sandwich-type aptamer and a DNA primer could form a long one-dimensional DNA which was treated with molybdate for generation of electrochemical current. According to the obtained results, the prepared aptasensor for HER2 detection in serum was highly correlated with ELISA measurements [21]. Finally, an aptamer-based colorimetric technique based on AuNPs was developed for HER2 detection. The aptamers were conjugated on AuNPs by adsorption-desorption colorimetric approach and HER2 selectively connected to the aptamers conjugated with AuNPs. Hence, LOD of 20.00 nM was obtained for HER2 detection [22].

Metal-organic frameworks (MOFs) are constructed by unification of metal ions with organic ligands having highly ordered structures. Due to specific surface area, low density, and porosity structure, MOFs have started to attract great attention [23]. They are used as a sensor amplification especially in drug delivery, electrochemistry applications, and energy storage [24–26]. In addition, MOFs have been currently utilized for significant substances' analyses [27]. Nonetheless, the incompatibility between metal nanoparticles such as AuNPs and MOFs occasionally result in sensor application problems. The incorporation of functional groups such as $–NH_2$ on metal nanoparticles can enhance the compatibility, providing a stable nanoparticles on MOFs. Hence, the materials including MOFs suggest a chance to prepare enzyme-free voltammetric sensors [28].

Metal chalcogenide as an inorganic molecule is composed of electropositive metal cation/cations and one chalcogen such as sulfides, selenides, and tellurides. Currently, due to the physico-chemical and electrochemical properties, metal chalcogenides have attracted attention. Generally, alkali/alkaline-earth metals and transition metals can form unique chalcogenides. Especially, empty d-orbitals in transition metals result in chalcogenide formation with different structures and composites such as binary ($MoSe_2$), ternary (MoSSe), and quaternary (Cu_2ZnSnS_4). In addition, the chalcogenides have perfect properties such as high conductivity and electrocatalytic activity, exclusive mechanical properties [29, 30]. Especially, Cu_2ZnSnS_4 has important interest because of its catalytic activity and large optical properties. Hence, Cu_2ZnSnS_4 has been currently used as a potential candidate in sensor applications [31].

g-C_3N_4 as a carbon-nitrogen based nanomaterial has currently attracted important interest owing to biocompatibility, specific surface area, low cytotoxicity, and chemical inertness. In addition, g-C_3N_4's modification with metal nanoparticles such as gold and platinum can significantly enhance catalytic performance and electron transfer in comparison with pristine g-C_3N_4 [32–34].

In this study in comparison with previous reports, HER2 detection has been performed for the first time with a higher precision and sensitivity using gold nanoparticles decorated Cu-MOF and Cu_2ZnSnS_4 NPs/Pt/g-C_3N_4 composite. Currently, metal nanoparticles and MOFs are embedded to enhance biosensors/sensors' performances. The traditional preparation techniques of metal nanoparticles/MOF composites are in situ preparation of nanoparticles into MOFs or nanoparticles' direct coatings on MOFs. We performed AuNPs coatings on MOFs via the stable hydrogen bonds between AuNPs and Cu-MOF, providing the high stability of AuNPs/Cu-MOF composite in comparison with the other metal nanoparticles/MOFs [35, 36]. In preparation of CZTS NPs/Pt/g-C_3N_4, one-pot hydrothermal method was carried out with minimal waste generation and high reaction efficiency. Hence, an environmentally friendly immunosensor was constructed for HER2 detection. Finally, the prepared immunosensor can provide a chance in the terms of early detection of breast cancer via this study.

Experimental section

Materials

Antigen HER2, capture antibody1-HER2 (primer, anti-HER2-Ab_1), detection antibody2-HER2 (seconder, anti-HER2-Ab_2), bovine serum albumin (BSA), Mucin 1 (MUC1), hepatitis B surface antigen (HBS), carcinoembryonic antigen (CEA), human immunoglobulin (IgG), melamine, chloroplatinic acid (H_2PtCl_6), thiourea (CH_4N_2S), $CuCl_2.2H_2O$, $Zn(CH_3COO)_2.2H_2O$, $SnCl_2.2H_2O$, gold (III) chloride trihydrate ($HAuCl_4{\cdot}3H_2O$), $Na_3C_6H_5O_7{\cdot}2H_2O$, L-cysteine, 1-ethyl-3-(3-dimethylaminopropyl) carbodiimide (EDC), N-hydroxysuccinimide (NHS), and $CuSO_4{\cdot}5H_2O$, 1,3,5-benzenetricarboxylic acid (BTCA) were purchased from Sigma-Aldrich. Phosphate-buffered saline (PBS, 0.1 M, pH 7.0) as supporting electrolyte and dilution buffer were also utilized.

Instrumentation

SEM and XRD images were obtained by using ZEISS EVO 50 SEM analytical microscopy and Rigaku X-ray diffractometer, respectively. JEOL 2100 TEM was utilized for obtaining TEM images. FTIR measurements were obtained by Bruker Tensor 27 FT-IR with DTGS detector. XPS analysis was carried out by using PHI 5000 Versa Probe. In addition, differential pulse voltammetry (DPV), CV, and EIS measurements were performed by using reference 600 workstation (Gamry, USA).

Preparation of Cu-MOF and AuNPs/Cu-MOF composite

$CuSO_4{\cdot}5H_2O$ solution (0.01 mmol), $NH_3{\cdot}H_2O$ (1.0 mL), and BTCA solution (0.01 mmol) were mixed at 25.0 °C under strong stirring for 45 min. Then, the prepared solution was transferred into Teflon autoclave at 100 °C during 12 h. After cooling treatment, the centrifugation at 10,000 rpm created a blue precipitation (***Cu-MOFs***). Cu-MOFs was washed with methanol and dried at 30.0 °C for 12 h [37].

AuNPs having the mean diameters of 20–25 nm were prepared by using $Na_3C_6H_5O_7{\cdot}2H_2O$ as reducing agent and $HAuCl_4{\cdot}3H_2O$ as precursor agent in harmony with literature [38]. Then, L-cysteine solution (0.1 mM, 250.0 μL) was added into AuNP solution under strong stirring during 6 h. After centrifugation treatment, ***–NH_2-AuNPs*** was collected and washed with methanol.

After the preparation of Cu-MOF (0.25 g) dispersion in ethanol (25.0 mL), NHS/EDC mixture (1:1, *v*/v) was added into the above dispersion, and the obtained solution was mixed for 30 min. Finally, ***AuNPs/Cu-MOF*** composite was formed with incorporation of –NH_2-AuNPs on Cu-MOFs. The preparation steps of AuNPs/Cu-MOF are shown on Scheme 1.

AuNPs/Cu-MOF composite as electrochemical sensor platform with anti-HER2-Ab_1 and antigen HER2 immobilizations

After dropping of AuNPs/Cu-MOF composite (25.0 μL) on clean glassy carbon electrode (GCE), the solvent on electrode surface was removed by IR lamp and AuNPs/Cu-MOF-modified GCE was developed (AuNPs/Cu-MOF/GCE). The immobilization process of primer antibody was carried out by amino gold affinity between anti-HER2-Ab_1 and AuNPs/Cu-MOF/GCE. For this aim, anti-HER2-Ab_1 dispersion (25.0 μL, 25.0 μg mL^{-1}) was dropped on AuNPs/Cu-MOF/GCE and left at 37.0 °C for 30 min [39] and tagged as ***anti-HER2-Ab_1/AuNPs/Cu-MOF/GCE***. Then, anti-HER2-Ab_1/AuNPs/Cu-MOF/GCE was washed with pH 7.0, 0.1 M PBS to remove non-interacting proteins at 37.0 °C for 60 min. In order to eliminate non-specific interactions, BSA (2.0% *w*/*v*) solution was incubated on anti-HER2-Ab_1/AuNPs/Cu-MOF/GCE at 37.0 °C for 30 min. After washing with pH 7.0, 0.1 M PBS and distinct antigen HER2 proteins having different concentration were immobilized on anti-HER2-Ab_1/AuNPs/Cu-MOF/GCE for 30 min at 37.0 °C and tagged as ***HER2/anti-HER2-Ab_1/AuNPs/Cu-MOF/GCE***. In order to remove non-interacting proteins, HER2/anti-HER2-Ab_1/AuNPs/Cu-MOF/GCE was washed with 0.1 M PBS (pH 7.0).

Preparation of g-C_3N_4, Pt/g-C_3N_4 composite, CZTS NPs, and CZTS NPs/Pt/g-C_3N_4

After the transfer of melamine (5.0 g) into an alumina crucible, the annealing treatment was applied at 600 °C during 3 h (rising rate of 3 °C min^{-1}). Then, the obtained bulk form was cooled to 25 °C and grounded in a mortal. Lastly, a faint-yellow polymeric powder (***g-C_3N_4***) was kept in a closed environment [40]. Pt/g-C_3N_4 composites including distinct Pt amounts were prepared by photo-deposition method, and H_2PtCl_6 was utilized as platinum source. After preparation of g-C_3N_4 solution (1.0 mg mL^{-1}) in the mixture of ultra-pure water/methanol (1:1), g-C_3N_4 solution was slowly added into H_2PtCl_6 dispersion (0.20 mg mL^{-1}) under ultra-sonication treatment for 30 min. After that, photo-deposition treatment was applied to g-C_3N_4/H_2PtCl_6 dispersion for 15 h. The obtained product was washed with ultra-pure water for three times and dried at 70 °C. Finally, the obtained powder was calcined at 550 °C for 1 h, providing ***5.0 wt% Pt/g-C_3N_4*** composite. The same procedure was applied to Pt/g-C_3N_4 composites with different Pt ratios, denoting as xPt/g-C_3N_4 where x was 5.0, 2.5, and 1.0 wt%.

In typical hydrothermal technique, $CuCl_2.2H_2O$ (4.0 mmol), $Zn(CH_3COO)_2.2H_2O$ (2.0 mmol), $SnCl_2.2H_2O$ (2.0 mmol), and CH_4N_2S (2.0 mmol) were dissolved in the mixture of ultra-pure water/ethanol (1:1) under strong stirring for 2 h at 70 °C. After transferring of the dispersion into a Teflon-autoclave, the heating treatment was applied at 250 °C for 15 h. After cooling process at 25 °C, the precipitates (***CZTS NPs***) were washed with ultra-pure water and stored in a closed environment [41].

The one-pot hydrothermal method was also utilized for the preparation of CZTS NPs/Pt/g-C_3N_4. Firstly, 5.0 wt% Pt/g-C_3N_4 (1.0 g) and CZTS NPs (10.0 g) were mixed in ultra-pure water/ethanol (1:1) under ultra-sonication for 45 min. After the suspension was transferred into a Teflon-autoclave, the heating treatment at 250 °C for 12 h was performed. Then, the product was cleaned with ultra-pure water and dried at 80 °C. Finally, the composite was calcined at 450 °C for 1 h, and the obtained composite was named as ***CZTS NPs/5.0 wt% Pt/g-C_3N_4***. The preparation steps of CZTS NPs/Pt/g-C_3N_4 are shown on Scheme 1.

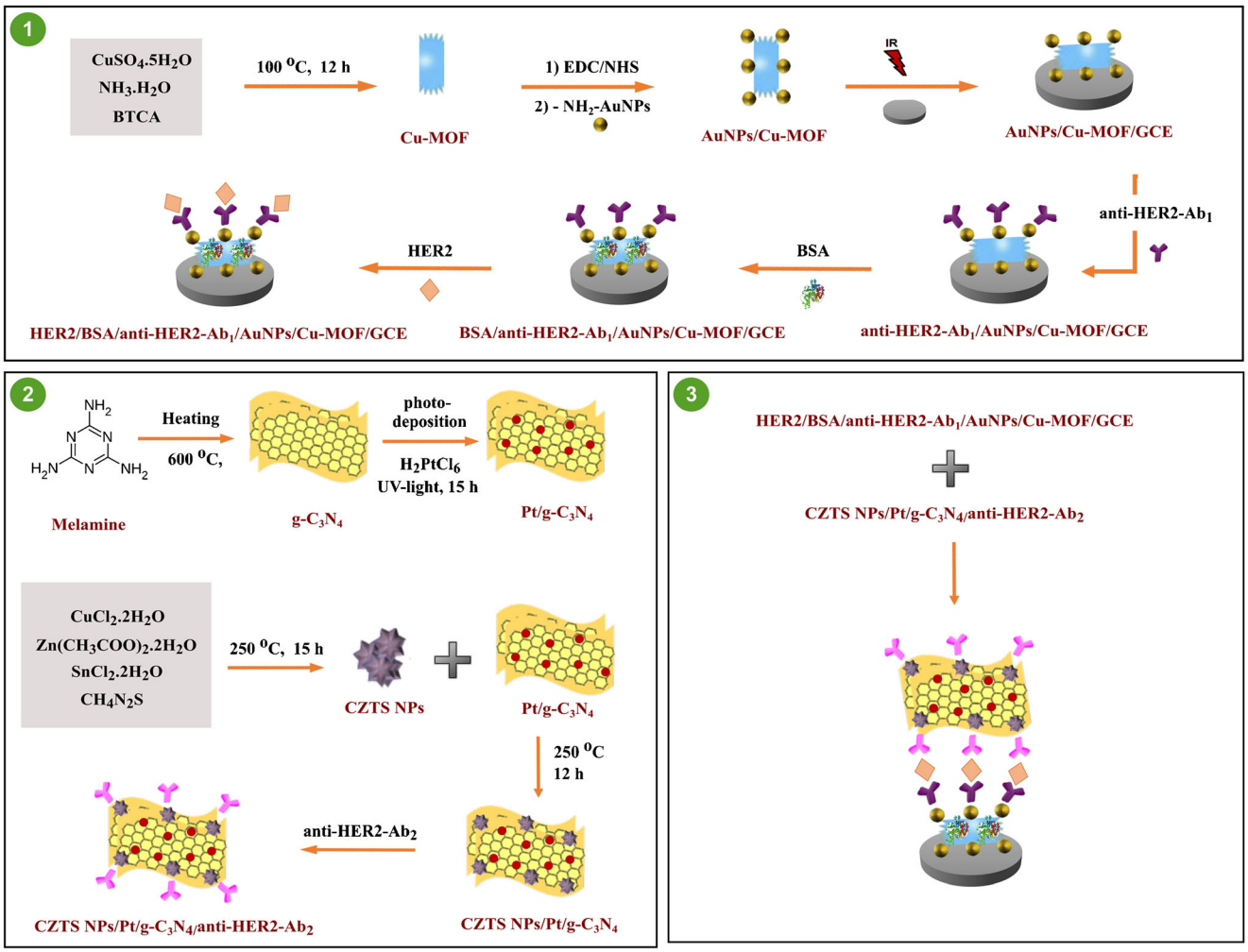

Scheme 1 Preparation procedure of electrochemical sensor platform, signal amplification and voltammetric immunosensor

CZTS NPs/Pt/g-C_3N_4 as signal amplification with anti-HER2-Ab_2 conjugation

After preparation of anti-HER2-Ab_2 (25.0 µL, 25.0 µg mL^{-1}), the seconder antibody was added into CZTS NPs/5.0 wt% Pt/g-C_3N_4 (25.0 µL, 30.0 mg mL^{-1}) dispersion under magnetic stirring at 37.0 °C for 30 min. Centrifugation process was carried out at 15,000 rpm during 45 min, and CZTS NPs/5.0 wt% Pt/g-C_3N_4 conjugated to anti-HER2-Ab_2 (***CZTS NPs/5.0 wt% Pt/g-C_3N_4/anti-HER2-Ab_2***) was preserved in pH 7.0, 0.1 M PBS.

Electrochemical measurements

Finally, electrochemical measurements were performed by the developed sandwich-type voltammetric immunosensor occurring the antibody-antigen interactions between CZTS NPs/5.0wt%Pt/g-C_3N_4/anti-HER2-Ab_2 and HER2/anti-HER2-Ab_1/AuNPs/Cu-MOF/GCE. For the immune reaction, CZTS NPs/5.0wt%Pt/g-C_3N_4/anti-HER2-Ab_2 dispersion (25.0 µL, 30 mg mL^{-1}) was dropped on sensor platform for 30 min. Lastly, the developed immunosensor (***CZTS NPs/5.0wt%Pt/g-C_3N_4/anti-HER2-Ab_2/HER2/anti-HER2-Ab_1/AuNPs/Cu-MOF/GCE***) was preserved in 0.1 M PBS. 0.1 M PBS (pH 7.0, 2.0 mL) as supporting electrolyte containing 1.0 mM H_2O_2 solution was prepared for electrochemical measurements. After working potential was applied in the range of 0.0/+0.6 V for DPV measurements, the voltammograms were recorded at +0.40 V. Before electrochemical measurements, argon gas (99.999%) was passed to remove dissolved oxygen for 15 min. In addition, the used parameters for DPV were frequency of 50 Hz, pulse amplitude of 20 mV and scan increment of 3 mV.

Sample preparation

HER2 free plasma samples were supplied from Blood Bank in TURKEY. Sample preparation protocol was explained in detail on Supplementary Data [42].

Results and discussion

Principle of voltammetric HER2 immunosensor based on AuNPs/Cu-MOF and CZTS NPs/Pt/g-C_3N_4

In the preparation of gold nanoparticles decorated Cu-MOF, benzene-1,3,5-tricarboxylate (BTC^{3-}) ligands serve as μ_4-bis-monodentate and bidentate coordination style to five-coordinated Cu(II) centers for trigonal bipyramidal formation. Four BTC^{3-} ligands also link to four Cu(II) centers into a 28-membered ring and Cl^- bridges two neighboring Cu(II) centers to create small 6-membered ring into 28-membered ring. Hence, 28-membered rings' growth via edge-sharing results in two-dimensional sheet along *ab*-plane. The amination reaction of AuNPs with L-cysteine forms $-NH_2$ groups on AuNPs. These $-NH_2$ groups create the stable hydrogen bonds between $-NH_2$ groups and –COO groups of Cu-MOF, providing the stabilization of the prepared AuNPs/Cu-MOF composite. In addition, –COO groups of Cu-MOF are activated by NHS/EDC mixture, and this activation provides the formation of AuNPs/Cu-MOF composite via amide bond. Finally, AuNPs/Cu-MOF serves as capture antibody1-HER2's immobilization via amino-gold affinity [43] and conductivity enhancement on sensor platform.

CZTS NPs/Pt/g-C_3N_4 composite as signal amplification is prepared by one-pot hydrothermal method with high efficiency between Pt/g-C_3N_4 and CZTS NPs. CZTS NPs/Pt/g-C_3N_4 composite is developed by the co-catalyst behavior of CZTS NPs and Pt NPs on g-C_3N_4 sheets, providing a high surface area and efficient charge separation. The synergistic effect between quaternary chalcogenide's electropositive metal cations and functional groups of detection antibody2-HER2 provided a stable conjugation by strong electrostatic interactions.

H_2O_2 as a redox probe was chosen because of its usage in biomolecules' medical diagnosis [44]. The continuous oxidation of H_2O_2 into O_2 at about +0.40 V was monitored by the prepared HER2 voltammetric immunosensor including antigen HER2 proteins with different concentrations.

Characterizations of gold nanoparticles decorated Cu-MOF (AuNPs/Cu-MOF) as sensor platform

XRD spectra were firstly obtained for characterizations of Cu-MOF and AuNPs/Cu-MOF (Fig. 1a). The characteristic peaks corresponding to Cu-MOF were observed in harmony with literature [45], confirming the high purity of the synthesized Cu-MOF. AuNPs/Cu-MOF also demonstrated an analogous XRD pattern, and the diffraction peaks located at 37.92° and 44.73° were attributed to (111) and (200) planes of cubic AuNPs [46, 47]. Thus, the similar and different XRD peaks showed AuNP presence and the structural stability of Cu-MOF in AuNPs/Cu-MOF. FTIR spectra of Cu-MOF and AuNPs/Cu-MOF showed that the absorption peaks belonging to BTC^{3-} ligand verified the presence of Cu-MOF (Fig. 1b). The peak at 1620 cm^{-1} attributing to OH–C=O stretching vibration and the absorption bands at 1500–1200 cm^{-1} corresponding to C=O of carboxyl groups indicated the incorporation of BTC^{3-} ligand on Cu-MOF and AuNPs/Cu-MOF composite [37]. The absorption bands attributing to C=C stretching of benzene structure were emerged at 1559 cm^{-1} and the absorption bands at 950–550 cm^{-1} were owing to C–H bending of benzene structure [48]. Finally, the band at 1650 cm^{-1} confirmed the presence of $-NH_2$ groups on AuNPs/Cu-MOF composite [49]. The morphological properties of Cu-MOF and AuNPs/Cu-MOF composite were also investigated by SEM measurements. According to Fig. 1c, Cu-MOF had column-type shape with average size of 120–410 nm. Lastly, many granular reliefs on Cu-MOF surface confirmed AuNPs' expansion on Cu-MOF (Fig. 1d).

Characterizations of g-C_3N_4, CZTS NPs, Pt/g-C_3N_4, and CZTS NPs/Pt/g-C_3N_4 composites as signal amplification

The morphological features of all samples were firstly investigated by using SEM measurements. Figure 2a demonstrated irregular two-dimensional nanosheet structure belonging to g-C_3N_4's bulk form. Nonetheless, CZTS NPs, having flower-like agglomerates, were comprised of many nanoplates with an average size of 120–140 nm (Fig. 2bs). SEM images (Figs. 2c, d, and e) of Pt/g-C_3N_4 composites showed curly, bulky, and two-dimensional nanosheet structures with an average size of 5–10 nm and Pt/g-C_3N_4 composites' structures were distinct in comparison with g-C_3N_4 including solid agglomerates. The well dispersion of Pt NPs on g-C_3N_4 surfaces was also seen, and no significant distinctions could be observed on morphological features of Pt/g-C_3N_4 composites with the increase of Pt amounts. According to SEM image (Fig. 2f) of CZTS NPs/5.0 wt% Pt/g-C_3N_4, the composite was composed of irregular agglomerates having spherical particles. Moreover, SEM image of CZTS NPs/5.0 wt% Pt/g-C_3N_4 showed the obvious incorporation and coating of flower-like CZTS NPs on 5.0 wt% Pt/g-C_3N_4 composite. After the conjugation of anti-HER2-Ab_2 on CZTS NPs/5.0 wt% Pt/g-C_3N_4 composite, the observed cloudy clusters indicated the specific interaction between seconder antibody and the final composite (Fig. 2g). According to EDS image (Fig. 2h), the presence of elements such as C, N, Pt, Cu, Zn, Sn and S was confirmed on composite structure.

Secondly, TEM measurements were carried out to investigate the morphological properties of all samples. The thread and porous structure was shown for g-C_3N_4 on Fig. S1a. According to Fig. S1b, the well dispersion of Pt NPs on g-C_3N_4 surface was demonstrated, and the lattice space of 0.21 nm belonging to (111) plane of Pt NPs was obtained.

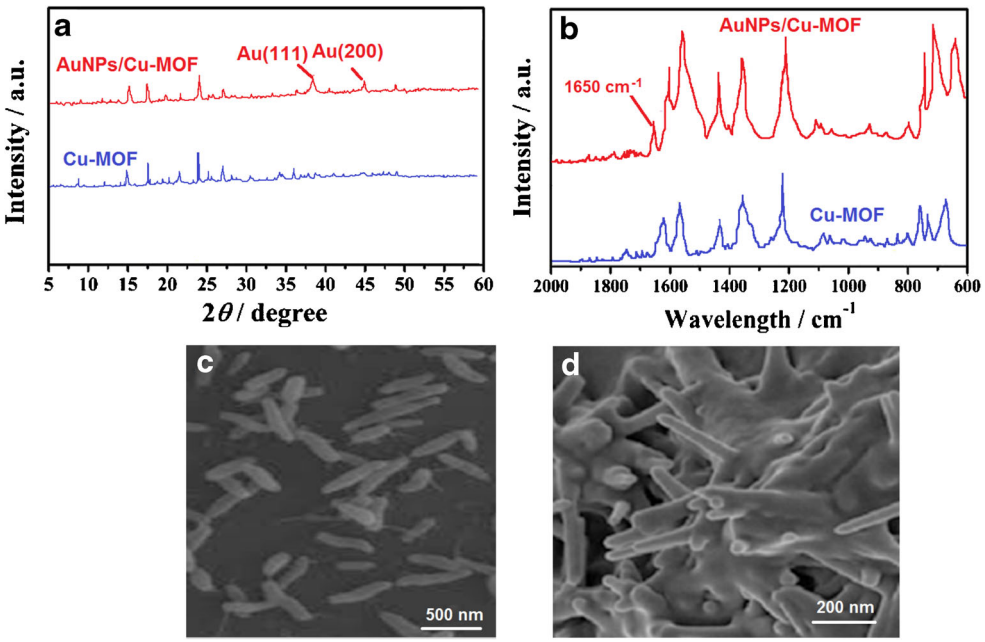

Fig. 1 (a) XRD patterns and (b) FTIR spectra of Cu-MOF and AuNPs/Cu-MOF composite, SEM images of (c) Cu-MOF and (d) AuNPs/Cu-MOF composite

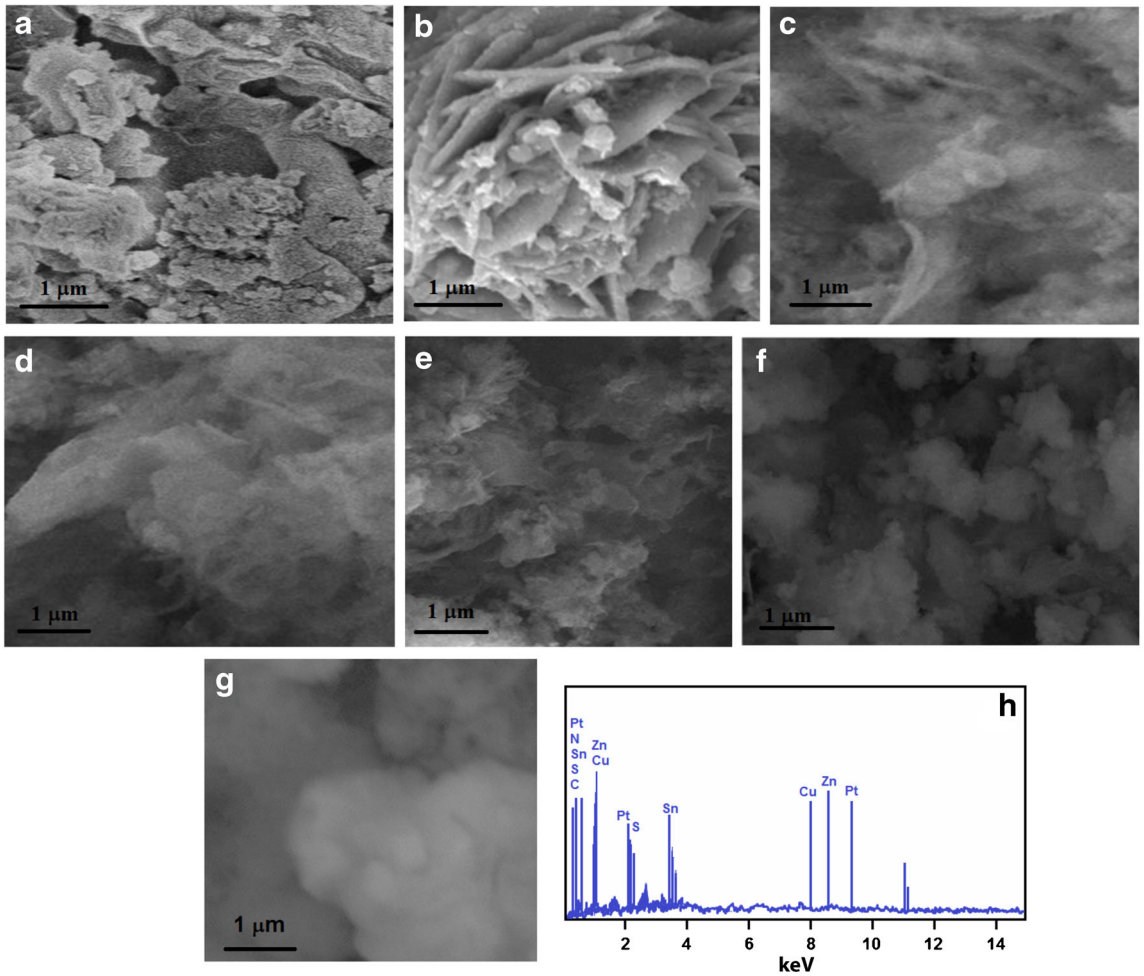

Fig. 2 SEM images of (a) g-C_3N_4, (b) CZTS NPs, (c) 1.0 wt% Pt/g-C_3N_4, (d) 2.5 wt% Pt/g-C_3N_4, (e) 5.0 wt% Pt/g-C_3N_4, (f) CZTS NPs/5.0 wt% Pt/g-C_3N_4, (g) CZTS NPs/5.0 wt% Pt/g-C_3N_4/anti-HER2-Ab_2, and (h) EDS spectra of CZTS NPs/5.0 wt% Pt/g-C_3N_4

Figure S1C verified flower-like agglomerates of CZTS NPs. Figure S1D shows that g-C_3N_4 having thread and porous structure acted as substrate for Pt NPs and CZTS NPs. The dark areas on the layered structure were also corresponded to the agglomerated CZTS NPs. Moreover, Pt NPs' distribution with an average size of 4–9 nm verified the decoration on g-C_3N_4 sheets. In addition, the close interface (demonstrated by white area line) between 5.0 wt% Pt/g-C_3N_4 and CZTS NPs resulted in effective charge transfer, and thus, the catalytic performance could be obviously improved.

FTIR spectra were obtained to investigate the structural properties relating to inter- and intra-bonds in g-C_3N_4, xPt/g-C_3N_4, and CZTS NPs/5.0 wt% Pt/g-C_3N_4 composite (Fig. S2A). Absorption bands related to amine groups and –OH stretching of adsorbed water were observed in the range of 3000–3400 cm^{-1} [50, 51]. Absorption bands in range of 1100–1650 cm^{-1} were corresponded to sp^3 C–N breathing and sp^2 C=N stretching modes [52] . In addition, the bands at 810–815 cm^{-1} and 890 cm^{-1} were attributed to triazine ring's breathing and N–H deformation modes, respectively [53]. Furthermore, the absorption bands at 441, 1088, and 1731 cm^{-1} were corresponded to stretching vibrations of Zn-N, C=S, and C=O, respectively, on CZTS NPs of composite [54, 55]. Thus, it is concluded that the structure of graphitic carbon nitride could not significantly change with the incorporation of CZTS NPs and PtNPs. In addition, the structural properties of g-C_3N_4, 5.0 wt% Pt/g-C_3N_4, and CZTS NPs/5.0 wt% Pt/g-C_3N_4 were highligted by XRD (Fig. S2b). The intensive peak at 27.30° was attributed to (002) plane of heptazine units of g-C_3N_4 [51]. Besides the peak located at 27.30°, two additional peaks at 39.70° and 45.80° were attributed to (111) and (200) planes of platinum, respectively, indicating Pt NPs' presence on g-C_3N_4. The peaks at 29.40°, 33.60°, 49.12°, and 55.22°, attributing to (112), (200), (220), and (312) planes, confirmed CZTS NP presence on composite.

XPS analysis was used to determine the chemical and electronic states of CZTS NPs/5.0 wt% Pt/g-C_3N_4 (Fig. 3). The survey spectra (Fig. 3A) demonstrated that 5.0 wt% Pt/g-C_3N_4 composite was composed of Zn2p, Sn3d, S2p, Cu2p, Pt4f, C1s, and N1s. Figure 3b showed Cu2p spectra including two peaks at 931.2 eV and 951.1 eV for $Cu2p_{3/2}$ and $Cu2p_{1/2}$, respectively. The oxidation state of Zn^{2+} was confirmed by two peaks at 1022.1 eV ($Zn2p_{3/2}$) and 1045.2 eV ($Zn2p_{1/2}$) (Fig. 3c), and the oxidation state of Sn^{4+} was verified by two characteristic peaks at 487.1 eV ($Sn3d_{5/2}$) and 494.9 eV ($Sn3d_{3/2}$) (Fig. 3d). Two obvious peaks at 160.5 eV and 162.1 eV were attributed to $S2p_{3/2}$ and $S2p_{1/2}$, respectively, indicating the presence of S^{2-} oxidation state (Fig. 3e). For C1s spectra, three peaks located at 284.8 eV, 286.2 eV, and 287.8 eV were corresponded to –C-NH_2, graphitic C-C, and –N-C=N bonds, respectively (Fig. 3f). The peaks at 398.5 eV, 399.5 eV, and 401.1 eV attributing to aromatic ring with -C-N=C, sp^3 bonded N-$[C]_3$ and –NH_2 groups were shown on N1s spectra (Fig. 3g) [56]. Finally, the peaks corresponding to 70.4 eV and 75.1 eV indicated $Pt4f_{7/2}$ and $Pt4f_{5/2}$, confirming Pt (II) state [57] (Fig. 3h). The binding energy of $Pt4f_{7/2}$ attributing to Pt^{2+} is generally located at 72.4 eV. Hence, the binging energy of $Pt4f_{7/2}$ containing in CZTS NPs/5.0 wt% Pt/g-C_3N_4 composite shifted to the lower energy, indicating electron transfer from g-C_3N_4 to Pt NPs [58]. Figure S3 demonstrated N_2 adsorption-desorption isotherms of g-C_3N_4, 5.0 wt% Pt/g-C_3N_4, and CZTS NPs/5.0 wt% Pt/g-C_3N_4 composite. According to Fig. S3, the whole samples had type IV isotherms, confirming mesoporous structures of samples. The specific surface areas (BET) were obtained as 9.12, 12.43, and 37.81 $m^2\ g^{-1}$ for g-C_3N_4, 5.0 wt% Pt/g-C_3N_4, and CZTS NPs/5.0 wt% Pt/g-C_3N_4 composite, respectively. About three times enhancement on BET surface area belonging to 5.0 wt% Pt/g-C_3N_4 and CZTS NPs/5.0 wt% Pt/g-C_3N_4 composite was owing to the incorporation of CZTS NPs. In addition, the pore volumes were calculated as 0.052, 0.098, and 0.177 $cm^3\ g^{-1}$ for for g-C_3N_4, 5.0 wt% Pt/g-C_3N_4, and CZTS NPs/5.0 wt% Pt/g-C_3N_4 composite, respectively. Hence, the electrochemical activity of the prepared composite may be increased by these large surface areas [59]. In literature, many catalysts such as Zn-MOF [60] and curcumin-MOF [61] were prepared according to their usage areas as photocatalysis and bioprocess. The surface areas of these catalysts can be higher and lower in comparison with CZTS NPs/5.0 wt% Pt/g-C_3N_4 composite. However, the one of basic aims of this study was to demonstrate the electrochemical biosensor usability and the textural properties of the prepared signal amplification (CZTS NPs/5.0 wt% Pt/g-C_3N_4). Especially, a perfect sensitivity with detection limit of 3.00 fg mL^{-1} for HER2 detection was obtained using AuNPs/Cu-MOF as sensor platform and CZTS NPs/5.0 wt% Pt/g-C_3N_4 as signal amplification in this study. Hence, this developed immunosensor may show a new way in real clinical cases.

Electrochemical characterizations of voltammetric immunosensor

Firstly, electrochemical characterizations of CZTS NPs/Pt/g-C_3N_4 composites containing different Pt/g-C_3N_4 amounts were performed in 1.0 mM $[Fe(CN)_6]^{3-}$ containing 0.1 M KCl by CV (Fig. S4A). Curve a of Fig. S4A showed a small anodic and cathodic peak signals by using bare GCE. Nonetheless, CZTS NPs/Pt/g-C_3N_4/GCE demonstrated the enhanced anodic and cathodic peak signals in 1.0 mM $[Fe(CN)_6]^{3-}$. Even CZTS NPs/5.0wt%Pt/g-C_3N_4 showed the highest electrocatalytic effect in comparison with composites including 2.5wt%Pt/g-C_3N_4 and 1.0wt%Pt/g-C_3N_4. Thus, we chose signal amplification including 5.0wt%Pt/g-C_3N_4 for

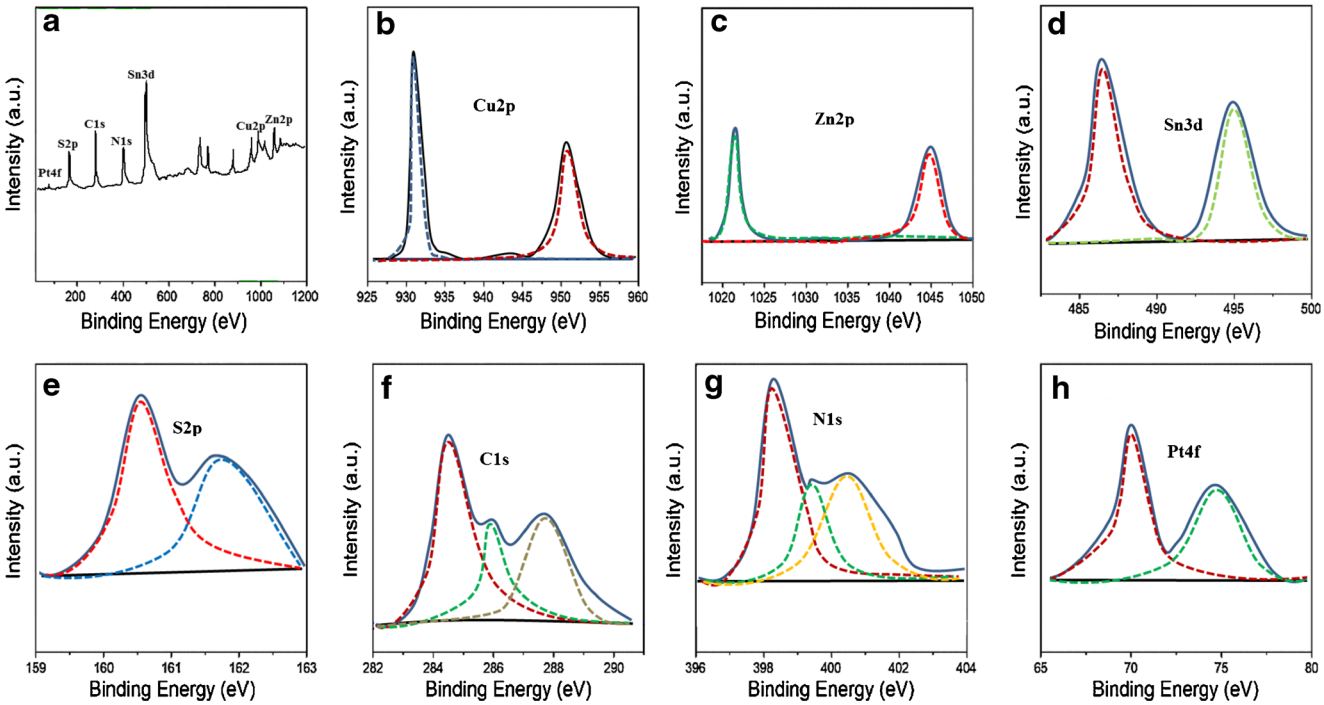

Fig. 3 (**a**) XPS survey spectra of 5.0 wt% Pt/g-C_3N_4 composite, High-resolution spectra of (**b**) Cu2p, (**c**) Zn2p, (**d**) Sn3d, (**e**) S2p, (**f**) C1s, (**g**) N1s, and (**h**) Pt4f

voltammetric immunosensor development and subsequent applications.

Secondly, electrochemical characterizations of the developed sensor platform were progressively carried out (Fig. S4b). Curve a of Fig. S4B showed a small anodic and cathodic peak signals by using bare GCE. The more pronounced anodic and cathodic peak signals were observed by Cu-MOF-modified GCE (Cu-MOFs/GCE) (curve b of Fig. S4B) owing to high surface area and more electrocatalytic tunable structure of Cu-MOFs [24, 62, 63]. Then, the increased anodic and cathodic peak signals were observed at AuNPs/Cu-MOF/GCE (curve c of Fig. S4B) because of the enhanced conductivity on electrode surface [64]. After anti-HER2-Ab_1's immobilization on AuNPs/Cu-MOF/GCE, an important decrease on signals of anodic and cathodic peaks was observed due to electron transfer prevention ability of capture antibody (curve d of Fig. S4B). Then, BSA's blocking effect caused the further decreases on the peak signals (curve e of Fig. S4B). Lastly, antigen HER2's immobilization on anti-HER2-Ab_1/AuNPs/Cu-MOF/GCE (curve f of Fig. S4B) made electron transfer more difficult in comparison with curve e of Fig. S4B. Hence, according to CV measurements, the incorporation of proteins such as primer, seconder, antigen, and BSA was successfully realized on sensor platform.

According to EIS measurements in 1.0 mM $[Fe(CN)_6]^{3-}$ containing 0.1 M KCl, the electrode conductivity on bare GCE surface (curve a of Fig. S4C) was gradually increased by Cu-MOFs/GCE (curve b of Fig. S4C) and AuNPs/Cu-MOF/GCE (curve c of Fig. S4C). Owing to primer anti-HER2-Ab_1 immobilization, the electrode resistance increased in harmony of CV results (curve d of Fig. S4C). Finally, electrochemical conductivity on electrode surface progressively decreased due to incorporation of BSA, antigen, and seconder (curve e-f of Fig. S4C). Hence, CV and EIS measurements showed that the accomplished sensor platform based on AuNPs/Cu-MOF composite was developed for novel HER2 detection.

Finally, various immunosensors including different signal amplifications such as 5.0wt%Pt/g-C_3N_4/anti-HER2-Ab_2 with CZTS NPs and without CZTS NPs were prepared to observe the effect of signal amplification (Fig. S5). Firstly, the previous prepared sensor platforms (AuNPs/Cu-MOF/GCE) including primer antibody and antigen HER2 were put on an immune reaction of 30 min with CZTS NPs/5.0wt%Pt/g-C_3N_4/anti-HER2-Ab_2, 5.0wt%Pt/g-C_3N_4/anti-HER2-Ab_2, and anti-HER2-Ab_2, respectively. The whole immunosensors were tested in 1.0 mM H_2O_2 in pH 7.0, 0.1 M PBS, and in the absence of H_2O_2. The signal amplification containing only anti-HER2-Ab_2 without any 5.0wt%Pt/g-C_3N_4 composite and CZTS NPs demonstrated a small signal for 1.0 mM H_2O_2 at about +0.40 V (curve b of Fig. S5). However, the signal amplifications containing 5.0wt%Pt/g-C_3N_4/anti-HER2-Ab_2 (curve c of Fig. S5) and CZTS NPs/5.0wt%Pt/g-C_3N_4/anti-HER2-Ab_2 (curve d of Fig. S5) showed the peak signals corresponding to 6.0 μA and

11.0 μA, respectively, at about +0.40 V. Because of the introduction of CZTS NPs, it caused a significant increase in electrochemical catalytic activity as a result of higher surface area. This synergistic effect relating to the interactions of CZTS NPs and Pt/g-C_3N_4 produced a combined effect greater than their separate effects, making the developed voltammetric immunosensor a potential candidate in clinical applications. In order to determine this synergistic effect, the specific surface areas of developed modified electrodes were calculated as 0.170 ± 0.04 cm^2 for bare GCE, 0.508 ± 0.02 cm^2 for 5.0wt%Pt/g-C_3N_4/GCE, and 0.938 ± 0.03 cm^2 for CZTS NPs/5.0wt%Pt/g-C_3N_4/GCE in the presence of 1.0 mM $[Fe(CN)_6]^{3-}$ solution by the equation (Randles–Sevcik) of $i_p = 2.69 \times 10^5\ A\ n^{3/2}\ D^{1/2}\ C\ v^{1/2}$, where i_p was current, C (mol cm^{-3}) was $[Fe(CN)_6]^{3-}$ concentration, v was scan rate (10–500 mV s^{-1}), and A was surface area (cm^2) ($n = 1$, D = 7.6×10^{-6} cm^2 s^{-1} for $[Fe(CN)_6]^{3-}$) [65]. According to the obtained results by the whole prepared signal amplifications, we preferred CZTS NPs/5.0wt%Pt/g-C_3N_4/anti-HER2-Ab_2 for subsequent immunosensor application.

Optimization for voltammetric measurements

The effects of pH, immune reaction time, H_2O_2, and CZTS NPs/5.0wt%Pt/g-C_3N_4/anti-HER2-Ab_2 solution concentrations were evaluated in detail on Fig. S6.

Linearity range

The obtained voltammograms at +0.4 V by developed immunosensor were shown on Fig. 4, and the inset of Fig. 4 demonstrated the obtained calicration equation as "y (μA) = 98.994x (pg mL^{-1}) + 1.095" based on linearity relation between immunosensor signals and HER2 concentrations. The quantification limit (LOQ) and LOD were calculated as 0.01 pg mL^{-1} and 3.00 fg mL^{-1}, respectively, by equations below:

$$LOQ = 10.0\ S/m \quad (1)$$

$$LOD = 3.3\ S/m \quad (2)$$

where S is the standard deviation of intercept and m is the slope of calibration equation. Table 1 showed the comparative studies in terms of sensitivity. Because of the synergistic effect between Pt NPs and CZTS NPs on g-C_3N_4 surface and high specific surface, the developed voltammetric immunosensor demonstrated the sensitive current signals, indicating a LOD of 3.00 fg mL^{-1}. We have also demonstrated the important advantages of HER2 voltammetric immunosensor in this study. Firstly, the prepared immunosensor with high selectivity was presented. Hence, the developed immunosensor had the potential to be used in place of conventional methods currently used. The immunosensor was also prepared under one-pot hydrothermal conditions in this study. During the preparation processes of sensor platform and signal amplification, little waste generation was also observed. Hence, cheaper, eco-friendly, and environmentally friendly immunosensor was prepared in this study. Moreover, the analysis process was performed in the shorter time in comparison with the other methods.

Recovery

Table S1 showed the recovery of HER2 in presence of pH 7.0, 0.1 M PBS containing 1.0 mM H_2O_2. The recovery was calculated by the eq. (3) below:

$$Recovery = Found\ HER2, pg\ mL^{-1} / Real\ HER2, pg\ mL^{-1} \quad (3)$$

Table S1 indicated recovery values close to 100.00%, confirming HER2 voltammetric immunosensor's high accuracy in complex protein medium. Furthermore, standard addition method was applied to plasma samples to investigate high selectivity properties of HER2 voltammetric immunosensor. Calibration equation of standard addition method was found as y (μA) = 98.981x (pg mL^{-1}) + 10.189. Hence, the close slopes between direct calibration and standard addition methods demonstrated that HER2 voltammetric immunosensor had perfect selectivity in complex plasma samples.

Selectivity, stability, reproducibility, and reusability

Six different protein solution mixtures including in HER2, HER2 + MUC1, HER2 + HBS, HER2 + CEA, HER2 + IgG, and HER2 + BSA were prepared to show the selectivity test of voltammetric immunosensor. Six different immunosensors were separately prepared by using above protein mixtures. After that, these 6 different immunosensors were applied to 1.0 mM H_2O_2 solution including in pH 7.0 and 0.1 M PBS (2.0 mL). According to Fig. S7A, 0.29% of relative standard deviation (RSD) verified high selectivity of prepared HER2 immunosensor.

The prepared HER2 immunosensor were preserved at 4.0 °C for 7 weeks and applied to 1.0 mM H_2O_2 solution for 7 weeks. According to Fig. S7B, the continuous acquired current signals during 7 weeks were about 99.02% of first current signal. In addition, the same stability tests were repeated for the prepared HER2 immunosensor at 25.0 °C for 7 weeks and 0.13% of RSD for immunosensor signals was obtained during 7 weeks at 25.0 °C. Hence, high stability at 4.0 and 25 °C showed that the prepared HER2 immunosensor was suitable for clinical applications. Twenty different HER2 immunosensors containing 0.100 pg mL^{-1} antigen HER2 were separately also prepared to demonstrate the

Table 1 Comparison of voltammetric HER2 immunosensor with other techniques

Material/method	Linear range	LOD	Ref.
Fe_3O_4@TMU-21	1.00–100.00 ng mL^{-1}	0.30 pg mL^{-1}	[3]
CdSe@ZnS	10.00–150.00 ng mL^{-1}	2.10 ng mL^{-1}	[66]
Streptavidin-alkaline phosphatase	7.50–50.00 ng mL^{-1}	0.16 ng mL^{-1}	[67]
Ab_2-PbS QDs	1.00–100.00 ng mL^{-1}	0.28 ng mL^{-1}	[68]
Label-free	10.00–70.00 ng mL^{-1}	1.60 ng mL^{-1}	[69]
Label-free	10.00–100.00 ng mL^{-1}	10.00 ng mL^{-1}	[70]
CdSe@ZnS quantum dots	0.50–50.00 ng mL^{-1}	0.29 ng mL^{-1}	[71]
Potentiometric	0.10–100.00 ng mL^{-1}	0.08 ng mL^{-1}	[72]
EIS	0.001–10.00 ng mL^{-1}	1.00 pg mL^{-1}	[73]
PbS QDs	1.00–100.00 ng mL^{-1}	0.28 ng mL^{-1}	[20]
CZTS NPs/5.0wt%Pt/g-C_3N_4	***0.01–1.00 pg mL^{-1}***	***3.00 fg mL^{-1}***	***This study***

reproducibility of HER2 immunosensor and utilized for 1.0 mM H_2O_2 solution. 0.73% of RSD showed the high reproducibility of the developed immunosensor. Finally, the reusability of HER2 immunosensor was presented in 1.0 mM H_2O_2 solution (Fig. S7C). One developed HER2 immunosensor was used at least 50 times and 0.92% of RSD for immunosensor signals was obtained. Thus, we successfully prepared HER2 immunosensor having high reusability in this study. DPV responses of the proposed HER2 immunosensor for investigations of selectivity, stability, reproducibility, and reusability were recorded at device parameters such as frequency of 50 Hz, pulse amplitude of 20 mV, and scan increment of 3 mV.

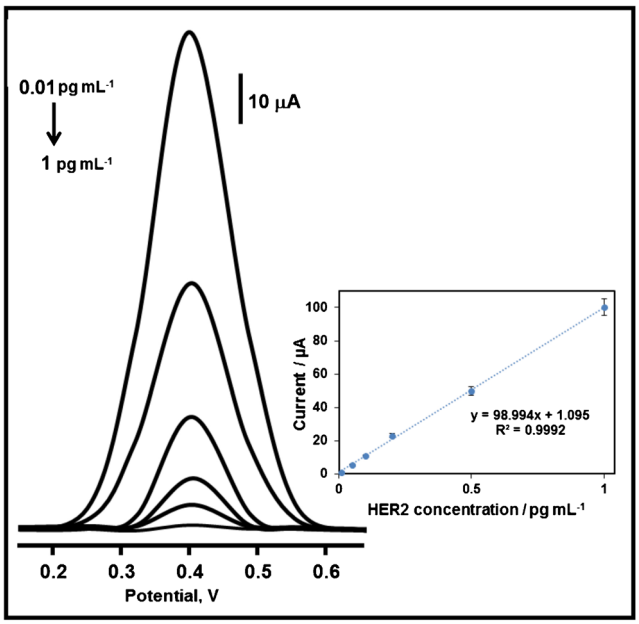

Fig. 4 Concentration effect (from 0.01 to 1.0 pg mL^{-1} HER2) on immunosensor signals, Inset: Calibration curve for voltammetric HER2 immunosensor (Potential range is 0.0/+0.6 V; Parameters are frequency of 50 Hz, pulse amplitude of 20 mV and scan increment of 3 mV)

Conclusions

In this report, a breast cancer biomarker HER2 detection based on gold nanoparticles decorated Cu-MOF as sensor platform and Cu_2ZnSnS_4 quaternary chalcogenide with platinum-dopped g-C_3N_4 composite as signal amplification was successfully realized by the prepared voltammetric immunosensor. Especially, HER2 voltammetric immunosensor demonstrated a satisfactory selectivity, stability, and reproducibility. The obtained calibration curve was established between 0.01 and 1.00 pg mL^{-1} and LOD of 3.00 fg mL^{-1} was observed. Moreover, due to easy, low-cost, and efficient preparation procedure for sensor platform and signal amplification, an environmentally friendly immunosensor was developed. In the same way, an alternative detection method was presented for clinical diagnosis by using breast cancer biomarker HER2 immunosensor. Nonetheless, the additional experiments using real blood samples (not HER2 free plasma samples) from healthy and breast cancer patients should be performed to show the prepared immunosensor's utility in real clinical cases.

Supplementary Information The online version contains supplementary material available at https://doi.org/10.1007/s00604-021-04735-y.

Acknowledgements Mehmet Lütfi YOLA would like to thank Turkish Academy of Sciences (TUBA- GEBIP) for their invaluable support.

Compliance with ethical standards

Conflict of interests The authors declare that they have no conflict of interests.

Conflict of interest The authors declare that they have no competing of interests.

References

1. Dennis J, Slamon PN, Chia S, Fasching PA, De Laurentiis M, Im S-A, Petrakova K, Bianchi GV, Esteva FJ, Mart'ın M, Nusch A, Sonke GS, De la Cruz-Merino L, Beck JT, Pivot X, Vidam G, Wang Y, Lorenc KR, Miller M, Taran T, Jerusalem G (2018) Phase III randomized study of Ribociclib and Fulvestrant in hormone receptor–positive, human epidermal growth factor receptor 2–negative advanced breast Cancer: MONALEESA-3. J Clin Oncol 36(24):2465–2472. https://doi.org/10.1200/JCO.2018.78.9909
2. Scaltriti M, Rojo F, Ocaña A, Anido J, Guzman M, Cortes J, Di Cosimo S, Matias-Guiu X, Ramon y Cajal S, Arribas J, Baselga J (2007) Expression of p95HER2, a truncated form of the HER2 receptor, and response to anti-HER2 therapies in breast Cancer. J Natl Cancer Inst 99(8):628–638. https://doi.org/10.1093/jnci/djk134
3. Ehzari H, Samimi M, Safari M, Gholivand MB (2020) Label-free electrochemical immunosensor for sensitive HER2 biomarker detection using the core-shell magnetic metal-organic frameworks. J Electroanal Chem 877:114722. https://doi.org/10.1016/j.jelechem.2020.114722
4. Chun L, Kim S-E, Cho M, W-s C, Nam J, Lee DW, Lee Y (2013) Electrochemical detection of HER2 using single stranded DNA aptamer modified gold nanoparticles electrode. Sens Actuators B Chem 186:446–450. https://doi.org/10.1016/j.snb.2013.06.046
5. Capobianco JA, Shih WY, Yuan QA, Adams GP, Shih WH (2008) Label-free, all-electrical, in situ human epidermal growth receptor 2 detection. Rev Sci Instrum 79(7):076101. https://doi.org/10.1063/1.2949831
6. Agersborg S, Mixon C, Nguyen T, Aithal S, Sudarsanam S, Blocker F, Weiss L, Gasparini R, Jiang S, Chen W, Hess G, Albitar M (2018) Immunohistochemistry and alternative FISH testing in breast cancer with HER2 equivocal amplification. Breast Cancer Res Treat 170(2):321–328. https://doi.org/10.1007/s10549-018-4755-5
7. Wolff AC, Hammond MEH, Hicks DG, Dowsett M, McShane LM, Allison KH, Allred DC, Bartlett JMS, Bilous M, Fitzgibbons P, Hanna W, Jenkins RB, Mangu PB, Paik S, Perez EA, Press MF, Spears PA, Vance GH, Viale G, Hayes DF (2013) Recommendations for human epidermal growth factor receptor 2 testing in breast Cancer: American Society of Clinical Oncology/College of American Pathologists Clinical Practice Guideline Update. Arch Pathol Lab Med 138(2):241–256. https://doi.org/10.5858/arpa.2013-0953-SA
8. Wang M, Hu M, Hu B, Guo C, Song Y, Jia Q, He L, Zhang Z, Fang S (2019) Bimetallic cerium and ferric oxides nanoparticles embedded within mesoporous carbon matrix: electrochemical immunosensor for sensitive detection of carbohydrate antigen 19-9. Biosens Bioelectron 135:22–29. https://doi.org/10.1016/j.bios.2019.04.018
9. Yola ML, Atar N (2020) Amperometric galectin-3 immunosensor-based gold nanoparticle-functionalized graphitic carbon nitride nanosheets and core–shell Ti-MOF@COFs composites. Nanoscale 12(38):19824–19832. https://doi.org/10.1039/D0NR05614F
10. Medetalibeyoglu H, Kotan G, Atar N, Yola ML (2020) A novel and ultrasensitive sandwich-type electrochemical immunosensor based on delaminated MXene@AuNPs as signal amplification for prostate specific antigen (PSA) detection and immunosensor validation. Talanta 220:121403. https://doi.org/10.1016/j.talanta.2020.121403
11. Karimi-Maleh H, Arotiba OA (2020) Simultaneous determination of cholesterol, ascorbic acid and uric acid as three essential biological compounds at a carbon paste electrode modified with copper oxide decorated reduced graphene oxide nanocomposite and ionic liquid. J Colloid Interface Sci 560:208–212. https://doi.org/10.1016/j.jcis.2019.10.007
12. Karimi-Maleh H, Karimi F, Alizadeh M, Sanati AL (2020) Electrochemical sensors, a bright future in the fabrication of portable kits in analytical systems. Chem Rec 20(7):682–692. https://doi.org/10.1002/tcr.201900092
13. Miraki M, Karimi-Maleh H, Taher MA, Cheraghi S, Karimi F, Agarwal S, Gupta VK (2019) Voltammetric amplified platform based on ionic liquid/NiO nanocomposite for determination of benserazide and levodopa. J Mol Liq 278:672–676. https://doi.org/10.1016/j.molliq.2019.01.081
14. Tahernejad-Javazmi F, Shabani-Nooshabadi M, Karimi-Maleh H (2019) 3D reduced graphene oxide/FeNi3-ionic liquid nanocomposite modified sensor; an electrical synergic effect for development of tert-butylhydroquinone and folic acid sensor. Compos B Eng 172:666–670. https://doi.org/10.1016/j.compositesb.2019.05.065
15. Khodadadi A, Faghih-Mirzaei E, Karimi-Maleh H, Abbaspourrad A, Agarwal S, Gupta VK (2019) A new epirubicin biosensor based on amplifying DNA interactions with polypyrrole and nitrogen-doped reduced graphene: experimental and docking theoretical investigations. Sens Actuators B Chem 284:568–574. https://doi.org/10.1016/j.snb.2018.12.164
16. Patris S, De Pauw P, Vandeput M, Huet J, Van Antwerpen P, Muyldermans S, Kauffmann J-M (2014) Nanoimmunoassay onto a screen printed electrode for HER2 breast cancer biomarker determination. Talanta 130:164–170. https://doi.org/10.1016/j.talanta.2014.06.069
17. Al-Khafaji QAM, Harris M, Tombelli S, Laschi S, Turner APF, Mascini M, Marrazza G (2012) An electrochemical immunoassay for HER2 detection. Electroanalysis 24(4):735–742. https://doi.org/10.1002/elan.201100501
18. Medetalibeyoglu H, Beytur M, Akyıldırım O, Atar N, Yola ML (2020) Validated electrochemical immunosensor for ultrasensitive procalcitonin detection: carbon electrode modified with gold nanoparticles functionalized sulfur doped MXene as sensor platform and carboxylated graphitic carbon nitride as signal amplification. Sens Actuators B Chem 319:128195. https://doi.org/10.1016/j.snb.2020.128195
19. Hartati YW, Letelay LK, Gaffar S, Wyantuti S, Bahti HH (2020) Cerium oxide-monoclonal antibody bioconjugate for electrochemical immunosensing of HER2 as a breast cancer biomarker. Sens Biosensing Res 27:100316. https://doi.org/10.1016/j.sbsr.2019.100316
20. Lah ZMANH, Ahmad SAA, Zaini MS, Kamarudin MA (2019) An electrochemical Sandwich Immunosensor for the detection of HER2 using antibody-conjugated PbS quantum dot as a label. J Pharm Biomed 174:608–617. https://doi.org/10.1016/j.jpba.2019.06.024
21. Shen C, Zeng K, Luo J, Li X, Yang M, Rasooly A (2017) Self-assembled DNA generated electric current biosensor for HER2 analysis. Anal Chem 89(19):10264–10269. https://doi.org/10.1021/acs.analchem.7b01747
22. Ranganathan V, Srinivasan S, Singh A, DeRosa MC (2020) An aptamer-based colorimetric lateral flow assay for the detection of human epidermal growth factor receptor 2 (HER2). Anal Biochem 588:113471. https://doi.org/10.1016/j.ab.2019.113471
23. Liao X, Fu H, Yan T, Lei J (2019) Electroactive metal–organic framework composites: design and biosensing application.

Biosens Bioelectron 146:111743. https://doi.org/10.1016/j.bios.2019.111743
24. Furukawa H, Cordova KE, O'Keeffe M, Yaghi OM (2013) The chemistry and applications of metal-organic frameworks. Science 341(6149):1230444. https://doi.org/10.1126/science.1230444
25. Zhou H, Zheng M, Tang H, Xu B, Tang Y, Pang H (2020) Amorphous intermediate Derivative from ZIF-67 and its outstanding Electrocatalytic activity. Small 16(2):1904252. https://doi.org/10.1002/smll.201904252
26. Abuzalat O, Wong D, Park SS, Kim S (2020) Highly selective and sensitive fluorescent zeolitic imidazole frameworks sensor for nitroaromatic explosive detection. Nanoscale 12(25):13523–13530. https://doi.org/10.1039/D0NR01653E
27. Chen J, Xu Q, Shu Y, Hu X (2018) Synthesis of a novel au nanoparticles decorated Ni-MOF/Ni/NiO nanocomposite and electrocatalytic performance for the detection of glucose in human serum. Talanta 184:136–142. https://doi.org/10.1016/j.talanta.2018.02.057
28. Chen Y-Z, Zhang R, Jiao L, Jiang H-L (2018) Metal–organic framework-derived porous materials for catalysis. Coord Chem Rev 362:1–23. https://doi.org/10.1016/j.ccr.2018.02.008
29. W-c P, Chen Y, X-y L (2016) MoS2/reduced graphene oxide hybrid with CdS nanoparticles as a visible light-driven photocatalyst for the reduction of 4-nitrophenol. J Hazard Mater 309:173–179. https://doi.org/10.1016/j.jhazmat.2016.02.021
30. J-w S, Y-w J, S-w P, Nah H, Moon T, Park B, Kim J-G, Kim YJ, Cheon J (2007) Two-dimensional Nanosheet crystals. Angew Chem Int Ed 46(46):8828–8831. https://doi.org/10.1002/anie.200703175
31. Badkoobehhezaveh AM, Abdizadeh H, Golobostanfard MR (2018) Electrophoretic behavior of solvothermal synthesized anion replaced Cu2ZnSn(SxSe1-x)4 films for photoelectrochemical water splitting. Int J Hydrog Energy 43(27):11990–12001. https://doi.org/10.1016/j.ijhydene.2018.04.140
32. Devaraji P, Gopinath CS (2018) Pt – g-C3N4 – (au/TiO2): electronically integrated nanocomposite for solar hydrogen generation. Int J Hydrog Energy 43(2):601–613. https://doi.org/10.1016/j.ijhydene.2017.11.057
33. Ong W-J, Tan L-L, Ng YH, Yong S-T, Chai S-P (2016) Graphitic carbon nitride (g-C3N4)-based photocatalysts for artificial photosynthesis and environmental remediation: are we a step closer to achieving sustainability? Chem Rev 116(12):7159–7329. https://doi.org/10.1021/acs.chemrev.6b00075
34. Zhang Y, Chai C, Zhang X, Liu J, Duan D, Fan C, Wang Y (2019) Construction of Pt-decorated g-C3N4/Bi2WO6 Z-scheme composite with superior solar photocatalytic activity toward rhodamine B degradation. Inorg Chem Commun 100:81–91. https://doi.org/10.1016/j.inoche.2018.12.019
35. Li C, Wu R, Zou J, Zhang T, Zhang S, Zhang Z, Hu X, Yan Y, Ling X (2018) MNPs@anionic MOFs/ERGO with the size selectivity for the electrochemical determination of H(2)O(2) released from living cells. Biosens Bioelectron 116:81–88. https://doi.org/10.1016/j.bios.2018.05.045
36. Liu CS, Sun CX, Tian JY, Wang ZW, Ji HF, Song YP, Zhang S, Zhang ZH, He LH, Du M (2017) Highly stable aluminum-based metal-organic frameworks as biosensing platforms for assessment of food safety. Biosens Bioelectron 91:804–810. https://doi.org/10.1016/j.bios.2017.01.059
37. Xu Q-Q, Liu B, Xu L, Jiao H (2017) Ionothermal synthesis and structural transformation targeted by ion exchange in metal-1,3,5-benzenetricarboxylate compounds. J Solid State Chem 247:1–7. https://doi.org/10.1016/j.jssc.2016.12.006
38. Yola ML, Atar N (2014) A novel voltammetric sensor based on gold nanoparticles involved in p-aminothiophenol functionalized multi-walled carbon nanotubes: application to the simultaneous determination of quercetin and rutin. Electrochim Acta 119:24–31. https://doi.org/10.1016/j.electacta.2013.12.028
39. La Belle JT, Demirok UK, Patel DR, Cook CB (2011) Development of a novel single sensor multiplexed marker assay. Analyst 136(7):1496–1501. https://doi.org/10.1039/c0an00923g
40. Yola ML, Eren T, Atar N (2016) A molecular imprinted voltammetric sensor based on carbon nitride nanotubes: application to determination of melamine. J Electrochem Soc 163(13):B588–B593. https://doi.org/10.1149/2.0311613jes
41. Yu X, Shavel A, An X, Luo Z, Ibáñez M, Cabot A (2014) Cu2ZnSnS4-Pt and Cu2ZnSnS4-au heterostructured nanoparticles for photocatalytic water splitting and pollutant degradation. J Am Chem Soc 136(26):9236–9239. https://doi.org/10.1021/ja502076b
42. Yola ML, Atar N (2019) Development of cardiac troponin-I biosensor based on boron nitride quantum dots including molecularly imprinted polymer. Biosens Bioelectron 126:418–424. https://doi.org/10.1016/j.bios.2018.11.016
43. Glišić BĐ, Rychlewska U, Djuran MI (2012) Reactions and structural characterization of 33(iii) complexes with amino acids, peptides and proteins. Dalton Trans 41(23):6887–6901. https://doi.org/10.1039/C2DT30169E
44. Stanković V, Đurđić S, Ognjanović M, Mutić J, Kalcher K, Stanković DM (2020) A novel nonenzymatic hydrogen peroxide amperometric sensor based on AgNp@GNR nanocomposites modified screen-printed carbon electrode. J Electroanal Chem 876:114487. https://doi.org/10.1016/j.jelechem.2020.114487
45. Sheberla D, Sun L, Blood-Forsythe MA, Er S, Wade CR, Brozek CK, Aspuru-Guzik A, Dincă M (2014) High electrical conductivity in Ni3(2,3,6,7,10,11-hexaiminotriphenylene)2, a semiconducting metal–organic Graphene analogue. J Am Chem Soc 136(25):8859–8862. https://doi.org/10.1021/ja502765n
46. Zhan W, Shu Y, Sheng Y, Zhu H, Guo Y, Wang L, Guo Y, Zhang J, Lu G, Dai S (2017) Surfactant-assisted stabilization of au colloids on solids for heterogeneous catalysis. Angew Chem Int Ed 56(16):4494–4498. https://doi.org/10.1002/anie.201701191
47. Maji SK, Sreejith S, Mandal AK, Ma X, Zhao Y (2014) Immobilizing gold nanoparticles in Mesoporous silica covered reduced graphene oxide: a hybrid material for cancer cell detection through hydrogen peroxide sensing. ACS Appl Mater Interfaces 6(16):13648–13656. https://doi.org/10.1021/am503110s
48. Abbasi AR, Karimi M, Daasbjerg K (2017) Efficient removal of crystal violet and methylene blue from wastewater by ultrasound nanoparticles cu-MOF in comparison with mechanosynthesis method. Ultrason Sonochem 37:182–191. https://doi.org/10.1016/j.ultsonch.2017.01.007
49. Feng Y, Jiang H, Li S, Wang J, Jing X, Wang Y, Chen M (2013) Metal–organic frameworks HKUST-1 for liquid-phase adsorption of uranium. Colloids Surf A Physicochem Eng Asp 431:87–92. https://doi.org/10.1016/j.colsurfa.2013.04.032
50. Yu J, Wang K, Xiao W, Cheng B (2014) Photocatalytic reduction of CO2 into hydrocarbon solar fuels over g-C3N4–Pt nanocomposite photocatalysts. Phys Chem Chem Phys 16(23):11492–11501. https://doi.org/10.1039/C4CP00133H
51. Raza A, Shen H, Haidry AA, Cui S (2019) Hydrothermal synthesis of Fe3O4/TiO2/g-C3N4: advanced photocatalytic application. Appl Surf Sci 488:887–895. https://doi.org/10.1016/j.apsusc.2019.05.210
52. Hao R, Wang G, Jiang C, Tang H, Xu Q (2017) In situ hydrothermal synthesis of g-C3N4/TiO2 heterojunction photocatalysts with high specific surface area for Rhodamine B degradation. Appl Surf Sci 411:400–410. https://doi.org/10.1016/j.apsusc.2017.03.197
53. Mousavi M, Habibi-Yangjeh A, Abitorabi M (2016) Fabrication of novel magnetically separable nanocomposites using graphitic carbon nitride, silver phosphate and silver chloride and their applications in photocatalytic removal of different pollutants using visible-

light irradiation. J Colloid Interface Sci 480:218–231. https://doi.org/10.1016/j.jcis.2016.07.021
54. Xu A, Tao H, Chen S, Zhu L, Zhao Y, Jiang J, Pan L, Tao J (2015) A novel approach to utilize thiol reduced graphene oxide as linker molecule for Cu2ZnSnS4 sensitized solar cell. Int J Hydrog Energy 40(46):15933–15939. https://doi.org/10.1016/j.ijhydene.2015.09.068
55. Suryawanshi M, Shin SW, Ghorpade U, Song D, Hong CW, Han S-S, Heo J, Kang SH, Kim JH (2017) A facile and green synthesis of colloidal Cu2ZnSnS4 nanocrystals and their application in highly efficient solar water splitting. J Mater Chem A 5(9):4695–4709. https://doi.org/10.1039/C7TA00257B
56. Raza A, Shen H, Haidry AA (2020) Novel Cu2ZnSnS4/Pt/g-C3N4 heterojunction photocatalyst with straddling band configuration for enhanced solar to fuel conversion. Appl Catal B 277:119239. https://doi.org/10.1016/j.apcatb.2020.119239
57. Ou M, Wan S, Zhong Q, Zhang S, Wang Y (2017) Single Pt atoms deposition on g-C3N4 nanosheets for photocatalytic H2 evolution or NO oxidation under visible light. Int J Hydrog Energy 42(44):27043–27054. https://doi.org/10.1016/j.ijhydene.2017.09.047
58. Nie L, Yu J, Li X, Cheng B, Liu G, Jaroniec M (2013) Enhanced performance of NaOH-modified Pt/TiO2 toward room temperature selective oxidation of formaldehyde. Environ Sci Technol 47(6):2777–2783. https://doi.org/10.1021/es3045949
59. Luo Y, Yan Y, Zheng S, Xue H, Pang H (2019) Graphitic carbon nitride based materials for electrochemical energy storage. J Mater Chem A 7(3):901–924. https://doi.org/10.1039/C8TA08464E
60. Akbarzadeh F, Motaghi M, Chauhan NPS, Sargazi G (2020) A novel synthesis of new antibacterial nanostructures based on Zn-MOF compound: design, characterization and a high performance application. Heliyon 6(1):e03231. https://doi.org/10.1016/j.heliyon.2020.e03231
61. Khandan FM, Afzali D, Sargazi G, Gordan M (2018) Novel uranyl-curcumin-MOF photocatalysts with highly performance photocatalytic activity toward the degradation of phenol red from aqueous solution: effective synthesis route, design and a controllable systematic study. J Mater Sci Mater Electron 29(21):18600–18613. https://doi.org/10.1007/s10854-018-9978-z
62. Li J-R, Sculley J, Zhou H-C (2012) Metal–organic frameworks for separations. Chem Rev 112(2):869–932. https://doi.org/10.1021/cr200190s
63. DeCoste JB, Peterson GW (2014) Metal–organic frameworks for air purification of toxic chemicals. Chem Rev 114(11):5695–5727. https://doi.org/10.1021/cr4006473
64. Mattioli IA, Baccarin M, Cervini P, Cavalheiro ÉTG (2019) Electrochemical investigation of a graphite-polyurethane composite electrode modified with electrodeposited gold nanoparticles in the voltammetric determination of tryptophan. J Electroanal Chem 835:212–219. https://doi.org/10.1016/j.jelechem.2018.12.056
65. Yola ML, Atar N (2019) Development of cardiac troponin-I biosensor based on boron nitride quantum dots including molecularly imprinted polymer. Biosens Bioelectron 126:418–424. https://doi.org/10.1016/j.bios.2018.11.016
66. Freitas M, Neves MMPS, Nouws HPA, Delerue-Matos C (2020) Quantum dots as nanolabels for breast cancer biomarker HER2-ECD analysis in human serum. Talanta 208:120430. https://doi.org/10.1016/j.talanta.2019.120430
67. Freitas M, Nouws HPA, Delerue-Matos C (2019) Electrochemical sensing platforms for HER2-ECD breast Cancer biomarker detection. Electroanalysis 31(1):121–128. https://doi.org/10.1002/elan.201800537
68. Lah Z, Ahmad SAA, Zaini MS, Kamarudin MA (2019) An electrochemical sandwich immunosensor for the detection of HER2 using antibody-conjugated PbS quantum dot as a label. J Pharm Biomed Anal 174:608–617. https://doi.org/10.1016/j.jpba.2019.06.024
69. Pacheco JG, Rebelo P, Freitas M, Nouws HPA, Delerue-Matos C (2018) Breast cancer biomarker (HER2-ECD) detection using a molecularly imprinted electrochemical sensor. Sens Actuators B Chem 273:1008–1014. https://doi.org/10.1016/j.snb.2018.06.113
70. Sharma S, Zapatero-Rodríguez J, Saxena R, O'Kennedy R, Srivastava S (2018) Ultrasensitive direct impedimetric immunosensor for detection of serum HER2. Biosens Bioelectron 106:78–85. https://doi.org/10.1016/j.bios.2018.01.056
71. Freitas M, Nouws HPA, Keating E, Fernandes VC, Delerue-Matos C (2020) Immunomagnetic bead-based bioassay for the voltammetric analysis of the breast cancer biomarker HER2-ECD and tumour cells using quantum dots as detection labels. Microchim Acta 187(3):184. https://doi.org/10.1007/s00604-020-4156-4
72. Ou D, Sun D, Lin X, Liang Z, Zhong Y, Chen Z (2019) A dual-aptamer-based biosensor for specific detection of breast cancer biomarker HER2 via flower-like nanozymes and DNA nanostructures. J Mater Chem B 7(23):3661–3669. https://doi.org/10.1039/C9TB00472F
73. Gu C, Guo C, Li Z, Wang M, Zhou N, He L, Zhang Z, Du M (2019) Bimetallic ZrHf-based metal-organic framework embedded with carbon dots: ultra-sensitive platform for early diagnosis of HER2 and HER2-overexpressed living cancer cells. Biosens Bioelectron 134:8–15. https://doi.org/10.1016/j.bios.2019.03.043